

Improved Sampling Schedules for Discrete Diffusion Models

Alberto Foresti ^{*1} Mustapha Bounoua ^{*1} Giulio Franzese ¹ Luca Ambrogioni ² Pietro Michiardi ¹

Abstract

Discrete diffusion models have emerged as a powerful paradigm for generative modeling on sequence data; however, the information-theoretic principles governing their reverse processes remain significantly less understood than those of their continuous counterparts. In this work, we bridge this gap by analyzing the reverse process dynamics through the lens of thermodynamic entropy production. We propose the entropy production rate as a rigorous proxy for quantifying information generation, deriving as a byproduct a bound on the Wasserstein distance between intermediate states and the data distribution. Leveraging these insights, we introduce two novel sampling schedules that are uniformly spaced with respect to their corresponding physics-inspired metrics: the Entropic Discrete Schedule (EDS), which is defined by maintaining a constant rate of information gain, and the Wasserstein Discrete Schedule (WDS), which is defined by taking equal steps in terms of the Wasserstein distance. We empirically demonstrate that our proposed schedules significantly outperform state-of-the-art strategies across diverse application domains, including synthetic data, music notation, vision and language modeling, consistently achieving superior performance at a lower computational budget.

1. Introduction

Drawing inspiration from non-equilibrium thermodynamics, diffusion models (Sohl-Dickstein et al., 2015; Ho et al., 2020; Song et al., 2021) learn to reverse a stochastic degradation process to unlock state-of-the-art generative capa-

¹Department of Data Science, EURECOM, 450 Route des Chappes, 06410 Biot, France ²Donders Institute for Brain, Cognition and Behaviour, Radboud University, Postbus 9102, 6500 HC Nijmegen, Netherlands. Correspondence to: Alberto Foresti, Mustapha Bounoua, Giulio Franzese, Pietro Michiardi <{alberto.foresti, mustapha.bounoua, giulio.franzese, pietro.michiardi}@eurecom.fr>, Luca Ambrogioni <luca.ambrogioni@donders.ru.nl>.

Preprint. February 9, 2026.

bilities. This paradigm has achieved remarkable success, mainly for continuous modalities such as vision (Ho et al., 2020; Ramesh et al., 2021; Rombach et al., 2022; Karras et al., 2022), audio (Kong et al., 2020), video synthesis (Ho et al., 2022) and multimodal data (Bao et al., 2023; Bounoua et al., 2023; Chen et al., 2024; Bounoua et al., 2025). Recently, this framework has also been extended to the discrete domain through the development of diffusion dynamics specifically adapted to sequence-based modalities (Austin et al., 2021; Campbell et al., 2022; Lou et al., 2024). Unlike Transformer-based autoregressive approaches (Vaswani et al., 2017), which are constrained by strictly causal dependencies and sequential, token-by-token generation, discrete diffusion models offer a more flexible paradigm. They enable parallel token generation and global context awareness, unlocking advanced features such as non-linear infilling, bidirectional sequence refinement, and improved controllability (Schiff et al., 2024a; Nisonoff et al., 2024; Li et al., 2024) that are less accessible to standard autoregressive architectures.

Recent work aims to improve discrete diffusion models training by designing noisy processes specifically tailored to discrete state spaces (Austin et al., 2021). Prominent approaches include *Masked Diffusion*, where sequence elements are gradually replaced by a special mask token until the signal is fully obscured, and *Uniform Diffusion*, where tokens are stochastically resampled until the sequence converges to a uniform categorical distribution. Recently, hybrid approaches have also emerged (Arriola et al., 2025). Lezama et al. (2022) extended the predictor-corrector framework (Song et al., 2021) to the discrete domain, while Zhao et al. (2024) introduced an informed corrector guided by the diffusion model to mitigate accumulating approximation errors. In parallel, research has focused on optimizing inference efficiency, exemplified by the fast solvers of Ren et al. (2025), as well as refining unmasking strategies for masked diffusion models (Sahoo et al., 2024; Ben-Hamu et al., 2025; Kim et al., 2025).

In particular, optimizing the sampling schedule of the reverse process has been identified as critical for efficiency (Chen, 2023). Addressing this, Park et al. (2024) analyzed the impact of compounding errors to propose a method for reducing generative costs, while Fu et al. (2025) introduced a distillation framework wherein a few-step student sampler

learns to align its intermediate score trajectory with that of a high-quality teacher. While these advancements are valuable, the field currently lacks a fundamental understanding of the inner dynamics governing these models. Specifically, it remains unclear how information flows, dissipates, and is reconstructed during the discrete diffusion reverse process. A theoretical grounding in these dynamics is essential not only for interpreting model behavior but also for deriving principled improvements to sampling schedules.

While diffusion models have been widely utilized to estimate information measures in both continuous (Franzese et al., 2023; Kong et al., 2022; Bounoua et al., 2024) and discrete settings (Foresti et al., 2025), the application of thermodynamic principles to analyze information storage (Premkumar, 2024) or optimize sampling strategies (Stancic et al., 2025) has been restricted to continuous diffusion models. In this work, we bridge this gap by extending this thermodynamic framework to the discrete setting. We summarize our primary contributions as follows:

- We derive the thermodynamic entropy production rate for discrete diffusion, establishing a rigorous framework that quantifies the generative information content of the reverse process.
- Building on this measure, we investigate a bound on the Wasserstein distance between intermediate distributions and the final data distribution, offering a theoretical lens to map the trajectory of the reverse process as it approaches the target state.
- We introduce two novel sampling schedules designed to be uniformly spaced with respect to the evolution of the reverse process. Entropic Discrete Schedule (EDS), separates time steps uniformly in entropy space, ensuring a constant rate of generative information gain. Wasserstein Discrete Schedule (WDS), separates time steps uniformly with respect to the Wasserstein distance, ensuring that the generative process takes steps of constant length in Wasserstein space.
- We empirically demonstrate that our proposed schedules enhance generation quality across diverse modalities (count data, music notation, vision and text), achieving superior performance with significantly lower computational cost.

2. Preliminaries

Consider a **Continuous Time Markov Chain (CTMC)** \vec{X}_t , with $t \in [0, T]$, defined over a finite state space $\chi = \{1, \dots, N\}$ and specified by the infinitesimal generators $\vec{Q}_t : [0, T] \rightarrow \mathbb{R}^{N \times N}$, where the diagonal entries satisfy $\vec{Q}_t(a, a) = -\sum_{a \neq b} \vec{Q}_t(a, b)$, with $\vec{Q}_t(a, b) \geq 0, a \neq b$.

As established by Anderson (2012), the time evolution of the probability distribution $\Pr(\vec{X}_t = x) \stackrel{\text{def}}{=} \vec{p}_t(x)$ satisfies the following **Ordinary Differential Equation (ODE)**: $\vec{p}_t = \vec{p}_0 + \int_0^t \vec{p}_s \vec{Q}_s ds$, where the initial conditions of the process \vec{p}_0 determine the distribution \vec{p}_t at any time t . A key property of **CTMCs** is that their time-reversed counterpart (Lou et al., 2024) also follows a **CTMC** with reverse generators \vec{Q}_t . Defining the time-reversed process as $\vec{p}_t \stackrel{\text{def}}{=} \vec{p}_{T-t}$, the reverse process evolves according to (Lou et al., 2024; Sun et al., 2023): $\vec{p}_t = \vec{p}_T + \int_0^t \vec{p}_s \vec{Q}_s ds$.

The reverse-time generator \vec{Q}_t is related to the forward generator \vec{Q}_t through the standard CTMC time-reversal formula. For $a \neq b$, $\vec{Q}_t(b, a) = \frac{\vec{p}_t(b)}{\vec{p}_t(a)} \vec{Q}_t(a, b)$, whereas $\vec{Q}_t(a, a) = -\sum_{b \neq a} \vec{Q}_t(b, a)$.

Under appropriate technical conditions on the forward rate matrix \vec{Q}_t (Lou et al., 2024), the terminal distribution \vec{p}_T converges to a known reference distribution π , independent of the initial data \vec{p}_0 . This property enables sampling from \vec{p}_0 by simulating a reverse-time **CTMC** via time-dependent generators (Sun et al., 2023; Kelly, 1981). In practice, the intractable density ratios $\frac{\vec{p}_t(b)}{\vec{p}_t(a)}$ governing reverse transitions are approximated by a score network $s_\theta^p(a, t)_b$, optimized via the **Diffusion Weighted Denoising Score Entropy (DWDSE)** loss (Lou et al., 2024). This network encodes the structural information necessary for reconstruction. While sampling typically relies on discretization (e.g., Euler solvers), optimizing these dynamics requires a rigorous understanding of how information is provided by the score network. In the following section, we quantify the information stored in the network parameters θ by applying entropic principles from stochastic thermodynamics. Specifically, we demonstrate how to measure this information storage and track its evolution as the reverse process converges to the final state.

3. Entropy Production in Discrete Diffusion

3.1. Entropy Production

The reverse generative trajectory can be analyzed through the lens of stochastic thermodynamics. In this framework, the irreversibility of the diffusion process is quantified by the *Entropy Production rate* \mathcal{H}^{tot} . Following the standard formulation (Seifert, 2005; Esposito & Van den Broeck, 2010; Premkumar, 2024), this is defined as the integral of the log ratio divergence between the backward path and the time-reversal of the forward path (See Section A.2):

$$\mathcal{H}^{\text{tot}} = \int_0^T \sum_{x,y} \overleftarrow{p}_t(x) \overleftarrow{Q}_t(x,y) \ln \left(\frac{\overleftarrow{p}_t(x) \overleftarrow{Q}_t(x,y)}{\overrightarrow{p}_{T-t}(y) \overrightarrow{Q}_{T-t}(x,y)} \right) dt. \quad (1)$$

In the context of continuous diffusion models, this quantity is termed *Neural Entropy* (Premkumar, 2024), representing the total information cost required to invert the corruption process. For reversible discrete processes, such as uniform diffusion, where the forward dynamics satisfy detailed balance, the total entropy production is finite. However, for non-reversible processes, such as absorbing diffusion, the reversal is singular: the transition rate from the absorbing state ‘[MASK]’ back to any data token is identically zero. This singularity causes the logarithmic probability ratio to diverge ($\mathcal{H}^{\text{tot}} \rightarrow \infty$), rendering the standard definition of total entropy ill-defined.

3.2. Decomposition of the total entropy production

To derive a finite quantity that works across different discrete processes, we adopt the adiabatic–non-adiabatic decomposition of entropy production for non-equilibrium Markov processes (Esposito & Van den Broeck, 2010; Hatano & Sasa, 2001). Within this framework, the total entropy production rate of a CTMC admits an exact decomposition into two contributions: the *Adiabatic Entropy Production* and the *Non-Adiabatic Entropy Production*, which follows from an explicit expansion of the logarithmic ratio of forward and backward path probabilities.

For a CTMC with time-dependent generator \overrightarrow{Q}_t , the corresponding entropy production rates read

$$\mathcal{H}^{\text{ad}}(t) = \sum_{x,y} \overleftarrow{p}_t(x) \overleftarrow{Q}_t(x,y) \ln \frac{\overleftarrow{Q}_t(x,y) \pi_t(x)}{\overleftarrow{Q}_t(y,x) \pi_t(y)}, \quad (2)$$

$$\mathcal{H}^{\text{na}}(t) = \sum_{x,y} \overleftarrow{p}_t(x) \overleftarrow{Q}_t(x,y) \ln \frac{\overleftarrow{p}_t(x) \pi_t(y)}{\overleftarrow{p}_t(y) \pi_t(x)}. \quad (3)$$

Here, π_t denotes the *instantaneous stationary distribution* of the generator \overrightarrow{Q}_t , defined by the invariance condition $\pi_t \overrightarrow{Q}_t = 0$ (Esposito & Van den Broeck, 2010). By construction, $\mathcal{H}^{\text{ad}}(t)$ quantifies the entropy production required to maintain the stationary non-equilibrium currents of the dynamics, while $\mathcal{H}^{\text{na}}(t)$ captures the relaxation of the system distribution \overrightarrow{p}_t toward the reference distribution π_t . Integrating over time yields the total entropy production:

$$\mathcal{H}^{\text{tot}} = \int_0^T \mathcal{H}^{\text{na}}(t) dt + \int_0^T \mathcal{H}^{\text{ad}}(t) dt \equiv \mathcal{H}^{\text{na}} + \mathcal{H}^{\text{ad}}, \quad (4)$$

where we leverage the identity $\overleftarrow{p}_t(y) \overleftarrow{Q}_t(y,x) = \overrightarrow{p}_{T-t}(x) \overrightarrow{Q}_{T-t}(x,y)$ (see Section A.3 for more details).

In uniform diffusion, the stationary distribution $\pi_t \equiv \pi$ is uniform, and detailed balance holds. Then, the adiabatic contribution vanishes ($\mathcal{H}^{\text{ad}} = 0$), and the total entropy production is entirely captured by the non-adiabatic term, thus in the case of uniform diffusion we have $\mathcal{H}^{\text{tot}} = \mathcal{H}^{\text{na}}$.

In contrast, for masked (absorbing) diffusion, the stationary distribution concentrates on the absorbing state, and detailed balance is violated. In this setting, the adiabatic entropy production diverges due to irreversible probability currents into the absorbing state, reflecting the infinite housekeeping cost of maintaining the absorbing prior. Crucially, the non-adiabatic entropy production \mathcal{H}^{na} remains finite, provided the marginal distributions \overleftarrow{p}_t retain full support over non-absorbing states. In the context of diffusion-based generative models, we identify the integrated non-adiabatic entropy production \mathcal{H}^{na} as the information theoretic cost associated with reshaping the probability mass of the model over time, independently of irreversible constraints imposed by the prior.

3.3. Wasserstein Speed Limit

The rate at which a generative model can transform an initial noise distribution \overrightarrow{p}_T into the data distribution \overrightarrow{p}_0 is fundamentally constrained by thermodynamic and geometric considerations. Let $\mathcal{W}(\overrightarrow{p}_0, \overrightarrow{p}_T)$ denote the L_1 -Wasserstein distance between the two distributions. Following the work by Van Vu & Saito (2023), this geometric transport distance is bounded by the total entropy production weighted by the mobility of the system (see Section A.4):

$$\mathcal{W}(\overleftarrow{p}_0, \overleftarrow{p}_T) \leq \int_0^T \sqrt{2 \mathcal{M}(t) \mathcal{H}^{\text{tot}}(t)} dt, \quad (5)$$

where the *dynamical state mobility* (Van Vu & Saito, 2023) $\mathcal{M}(t)$ captures the strength of the state transitions under the CTMC generator \overrightarrow{Q}_t . Conveniently, Van Vu & Saito (2023) show that :

$$\mathcal{M}(t) \leq \frac{\mathcal{A}(t)}{2} = \sum_{x,y} \overleftarrow{Q}(x,y) \overleftarrow{p}_t(y) \quad (6)$$

While the above bound holds for reversible dynamics with finite total entropy production, such as uniform diffusion, it diverges for masked absorbing processes due to irreversible housekeeping currents. However, probability transport remains finite and is driven primarily by the non-adiabatic entropy production (Yoshimura et al., 2023). In our experiments, we found that an extremely practical surrogate for

this bound, using only non-adiabatic entropy production, provides the best empirical performance, as discussed in Section A.4.

Intuitively, these inequalities impose a *speed limit* on generative dynamics: for a fixed geometric displacement $\mathcal{W}(\overleftarrow{p}_0, \overleftarrow{p}_T)$, the minimal entropy production \mathcal{H}^{tot} determines the fastest possible trajectory through probability space. Equivalently, minimizing \mathcal{H}^{tot} corresponds to following the *optimal transport geodesic* between noise and data, achieving the most efficient generative transformation under the constraints of the [CTMC](#) dynamics.

3.4. Estimation of Neural Entropy

We consider the reverse process to be simulated using a neural network trained to approximate the probability ratio $s_\theta^p(x, y)$ (see Section 2). We aim to estimate the non-adiabatic neural entropy $\mathcal{H}_\theta^{\text{na}}$ as a proxy for the information produced by the network during the generative process.

Information generation is quantified by the estimated non-adiabatic entropy production rate. Assuming the stationary distribution terms vanish (as in uniform or absorbing diffusion), the non-adiabatic entropy for the discrete diffusion parameterization in (Lou et al., 2024) can be computed as:

$$\mathcal{H}_\theta^{\text{na}}(t) = - \sum_{x,y} \overleftarrow{p}_t(x) \overleftarrow{Q}_t(x, y) \ln s_\theta^p(x, y). \quad (7)$$

The total non-adiabatic entropy generated over the full trajectory is obtained by integrating this rate over time. Replacing the summation with an expectation over the generated samples yields the *Total Non-Adiabatic Neural Entropy*:

$$\mathcal{H}_\theta^{\text{na}} = - \int_0^T \mathbb{E}_{x \sim \overleftarrow{p}_t} \left[\sum_y \overleftarrow{Q}_t(x, y) \ln s_\theta^p(x, y) \right] dt. \quad (8)$$

Once this non adiabatic entropy production is computed, the speed limit on the generative process, expressed as a bound on the Wasserstein distance, can be derived by Equation (5) which we refer to as $\mathcal{W}_\theta(\overleftarrow{p}_0, \overleftarrow{p}_t)$. These quantities provide a computable measure of the progress of the reverse process in reshaping probability mass, grounded in the thermodynamic framework of (Hatano & Sasa, 2001; Esposito & Van den Broeck, 2010). Detailed derivations are provided in Section A.5.

4. Improved Sampling Schedules for Discrete Diffusion models

The efficacy of discrete diffusion sampling depends critically on the *time schedule*, which dictates the discretization grid for the reverse process. While efficient numerical integrators such as τ -leaping (Campbell et al., 2022; Lou et al.,

2024) allow for practical inference by updating multiple tokens in parallel, they rely on the assumption that the transition rates remain approximately constant within each time step. The validity of this assumption is entirely controlled by the chosen schedule, which governs the rate of noise removal and, consequently, the magnitude of the distributional shift at each step.

Standard approaches to scheduling typically impose fixed, heuristic functional forms on the noise dynamics. Common baselines include Linear schedules, which are standard in masked modeling. However, these agnostic schedules advance time based on kinematic constraints rather than the information complexity of the generation. This misalignment often leads to inefficient allocation of the computational budget: the sampler may waste steps resolving trivial noise while moving too aggressively through critical phase transitions where semantic structure is established. Such aggressive discretization in high-entropy regions may yield approximation errors, leading to mode collapse (Park et al., 2024). We propose that the improved time schedule should be derived not from heuristic functions, but from the thermodynamic properties of the generative process itself.

As observed in Figures 1 and 8, the information content generated during the reverse process quantified by the non adiabatic entropy production rate $\mathcal{H}_\theta^{\text{na}}(t)$ evolves in a non-linear manner, subject to the prior diffusion framework and the data distribution. This non-linearity is mirrored in the transport dynamics: as the generation progresses toward the target state, it proceeds with a non-constant velocity, as evidenced by the Wasserstein distance in Figure 1. Consequently, we propose a physically motivated scheduling approach, where the time discretization is governed by the intrinsic progress of the generative process. We introduce two sampling strategies: the [Entropic Discrete Schedule \(EDS\)](#), which adapts to the information load, and the [Wasserstein Discrete Schedule \(WDS\)](#), which adapts to the transport velocity in the Wasserstein metric.

4.1. Cumulative Progress

To quantify the progression of the diffusion process, we define the *Cumulative Progress* function $\mathcal{C}(t)$. This function measures the accumulation of a physical quantity (information or distance) from the initial state ($t = 0$) up to the current noise level t :

$$\mathcal{C}(t) = \int_0^t \rho(\tau) d\tau, \quad (9)$$

where $\rho(\tau)$ represents the instantaneous rate of change of the chosen metric. Assuming $\rho(\tau) \geq 0$, $\mathcal{C}(t)$ is non-decreasing and bounded by $\mathcal{C}(T)$, it allows to map the diffusion time $t \in [0, T]$ to the progress domain $\mathcal{C} \in [0, \mathcal{C}_{\text{total}}]$, with $\mathcal{C}_{\text{total}} \stackrel{\text{def}}{=} \mathcal{C}(T)$.

The objective of our improved scheduling is to find a time discretization $\{t_k\}_{k=0}^K$ such that the progress between consecutive steps is uniform. We define the Warping Function $\Phi : [0, T] \rightarrow [0, 1]$ as the normalized cumulative progress:

$$\Phi(t) = \mathcal{C}(t)/\mathcal{C}(T). \quad (10)$$

Physically, $\Phi(t)$ represents the ratio of the total budget (information generated or distance traversed) that has been consumed by time t . The improved schedule is obtained by inverting this warping function. Assuming Φ is strictly increasing, for K generation steps we define the discrete time points t_k as uniform samples in the progress domain:

$$t_k = \Phi^{-1}(k/K), \quad \text{for } k = 0, \dots, K. \quad (11)$$

Next, we cast this framework for our proposed schedules.

4.2. Entropic Discrete Schedule (EDS)

The **EDS** is derived from thermodynamic principles. We identify the instantaneous rate of non-adiabatic entropy as the information load of the generative process:

$$\rho_{\text{EDS}}(t) \stackrel{\text{def}}{=} \mathcal{H}_{\theta}^{\text{na}}(t). \quad (12)$$

Here, $\mathcal{H}_{\theta}^{\text{na}}(t)$ can be obtained from Equation (7). $\rho_{\text{EDS}}(t)$ represents the density of useful information retrieved by the model at time t . This schedule slows down time during phase transitions where information gain is high (Figure 1) and speeds up during low-information regimes, ensuring a constant information rate.

4.3. Wasserstein Discrete Schedule (WDS)

The **WDS** can be viewed from optimal transport geometry. We identify the distance to the data manifold as the progress metric. We define the rate $\rho_{\text{WDS}}(t)$ as the instantaneous Wasserstein distance rate:

$$\rho_{\text{WDS}}(t) \stackrel{\text{def}}{=} \frac{d}{dt} \mathcal{W}(\overleftarrow{p}_0, \overleftarrow{p}_t), \quad (13)$$

where $\mathcal{W}(\overleftarrow{p}_0, \overleftarrow{p}_t)$ denotes the time-dependent Wasserstein bound up to time t , generalizing Equation (5). Consequently, the cumulative function $\mathcal{C}_{\text{WDS}}(t)$ is given by the distance itself:

$$\mathcal{C}_{\text{WDS}}(t) = \mathcal{W}(\overleftarrow{p}_0, \overleftarrow{p}_t). \quad (14)$$

This schedule ensures that the generative process takes steps of equal geometric length in probability space, corresponding to a *constant transport speed*.

4.4. Implementation Details

Algorithm 1 outlines our method, which is practical and requires no additional training. Using a pre-trained model

Algorithm 1 Our Method: Improved Sampling Schedule

Require: Pre-trained Model θ , Dataset Batch \mathbf{X}_0 , Diffusion range $[0, T]$, Steps K .
Ensure: Discrete schedule $\{t_k\}_{k=0}^K$.

```

1: 1. Estimate Neural Entropy
2: Define fine grid  $\tau_i \in [0, T]$  (e.g.,  $N = 1000$  points).
3: for each  $\tau_i$  do
4:   Sample batch  $x_{\tau_i} \sim \overrightarrow{p}_{\tau_i}$ 
5:   Estimate  $\mathcal{H}_{\theta}^{\text{na}}(\tau_i)$  using Equation (8)
6: end for
7: if Strategy is EDS then
8:   Integrate  $\mathcal{H}_{\theta}^{\text{na}}(\tau)$  to obtain progress curve  $\mathcal{C}(\tau)$ .
9: else if Strategy is WDS then
10:   $\mathcal{C}(\tau) \leftarrow \mathcal{W}(\overleftarrow{p}_0, \overleftarrow{p}_{\tau})_{\theta}$  {Wasserstein distance using
     $\mathcal{H}_{\theta}^{\text{na}}(\tau)$  (Equation (24))}
11: end if
12:  $\Phi(\tau) \leftarrow \mathcal{C}(\tau)/\mathcal{C}(T)$  {Normalize to  $[0, 1]$ }
13: 2. Construct Schedule
14: for  $k = 0$  to  $K$  do
15:    $t_k \leftarrow \Phi^{-1}(k/K)$  {Uniform sampling in intrinsic
    space}
16: end for
17: return  $\{t_k\}$ 

```

and a representative batch from the training data, we first estimate the neural entropy rate $\mathcal{H}_{\theta}^{\text{na}}(t)$ across the diffusion trajectory. We then define a cumulative progress function based either on the entropy rate itself (informational progress, **EDS**) or on a Wasserstein distance proxy derived from it (geometric progress, **WDS**) map physical time to an intrinsic domain. Finally, by inverting this function, we obtain a new time schedule that ensures uniform sampling steps within this intrinsic space and is compatible with any sampler (e.g., the Euler τ -leaping (Campbell et al., 2022)).

5. Experiments

In this section, we evaluate our proposed sampling schedules, **EDS** and **WDS**, across various datasets and models. We begin by analyzing the generative dynamics of discrete diffusion models under different kernels (Uniform and Absorbing) to establish a foundational understanding. This analysis is made possible via the thermodynamic-inspired quantities derived in Section 3. We then compare our schedules against the standard uniform sampling baseline (constant intervals) and the JYS by Park et al. (2024), which derives a schedule based on the compounding error of information. Following (Park et al., 2024), we utilize pretrained models for all experiments, as our method requires no additional training; instead, it derives a physically intrinsic schedule rooted directly in the dynamics of the pretrained model (see Algorithm 1). We assess performance against

the computational budget (Number of Function Evaluations, or NFEs) across multiple domains: synthetic count data, monophonic music, vision and language modeling. We report the experimental details in Section A.6 and additional results in Section B.

5.1. Entropic and Geometric Dynamics

Following (Premkumar, 2024), we validate our thermodynamic quantities on a tractable binomial distribution ($n = 14, p = 0.5$). We train models using the DWDSE loss and geometric noise ($\sigma_{\max} = 5.0, \sigma_{\min} = 0.01$). Figure 1 compares the resulting dynamics under Uniform and Absorb diffusion kernels.

Discussion. The Non-Adiabatic Entropy Rate $\mathcal{H}_{\theta}^{\text{na}}(t)$ reveals the rate of information gain, demonstrating that generation is highly non-linear. Under the Uniform kernel, information flow follows a bell-shaped curve, peaking at $t \approx 0.6$. This identifies a critical “phase transition” where semantic structure is resolved, which linear schedules tend to undersample. In contrast, the absorbing kernel shows an exponential spike near $t = 1$, indicating that information emerges abruptly at the very end of the process. This sharp difference highlights why a single fixed schedule cannot optimally serve both dynamics. Geometrically, Wasserstein measures mirror the entropic findings. The transport velocity (Row c) peaks alongside information gain, confirming that major geometric shifts align with semantic resolution. Crucially, this non-linearity of the dynamics persists across real-world datasets and pre-trained architectures, as validated by the extended analysis in Figure 8. The Model estimation closely tracks the Ground Truth across all metrics, validating the use of the pre-trained network for estimating the dynamics of the diffusion model.

5.2. COUNT DATA

Following Park et al. (2024), we evaluate our sampling schedules on a generated countdown dataset. Tokens $X \in \{0, \dots, 31\}$ follow a deterministic rule where each value decrements the previous one until reaching zero, at which point it resets to a uniform random value. A discrete diffusion model with an absorbing state (Lou et al., 2024) was trained. Performance is measured by the *rule violation rate* the proportion of generated tokens that fail to adhere the rule of generation. As illustrated in Figure 3, our proposed schedules significantly outperform the uniform baseline across all computational budgets.

Specifically, WDS and EDS achieve a dramatic reduction in error rates, particularly in the challenging low-NFEs regime (2–16 stpdf). For instance, at just 8 NFEs, WDS matches the performance that Uniform schedule requires ≈ 32 NFEs to achieve, representing a $4\times$ inference speedup. Furthermore, WDS consistently surpasses the JYS schedule (Park et al.,

2024), maintaining its advantage even at larger NFEs (> 32 stpdf). These results demonstrate that our sampling schedules achieve a significant incremental improvement in the performance-budget trade-off.

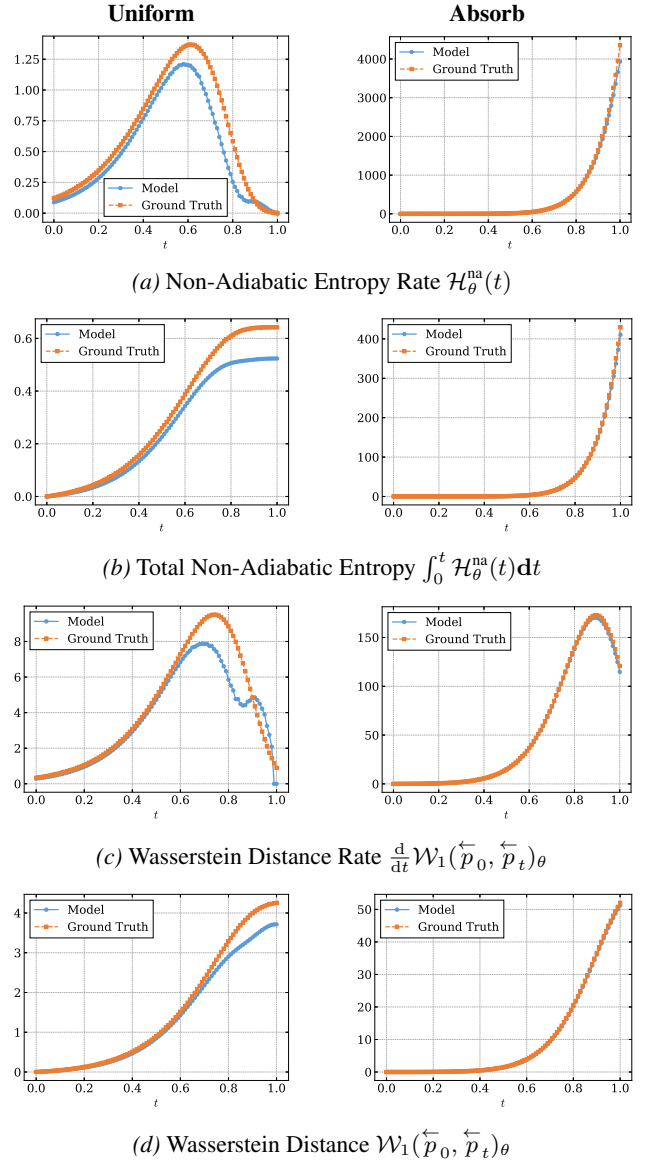


Figure 1. Comparison of entropy and Wasserstein dynamics over time. The left column displays results for Uniform diffusion, while the right column shows Absorb diffusion, both trained on a toy binomial distribution. Each plot presents the ground truth values alongside the model’s estimates.

5.3. MONOPHONIC MUSIC

We evaluate conditional music generation on the Lakh piano-roll dataset (Raffel, 2016; Dong et al., 2018), employing the uniform transition model from Campbell et al. (2022). Conditioning on two bars, we generate the subsequent 14 bars (256 total timestamppdf). Performance is assessed using

the outlier score and the Hellinger distance between note distributions at reduced NFEs (2 to 64) relative to a high-fidelity baseline (NFE 512). Results in Figure 2 demonstrate that our proposed schedules, **EDS** and **WDS**, significantly outperform the uniform sampling baseline. Notably, **EDS** matches the quality of 512-NFE samples at a fraction of the cost.

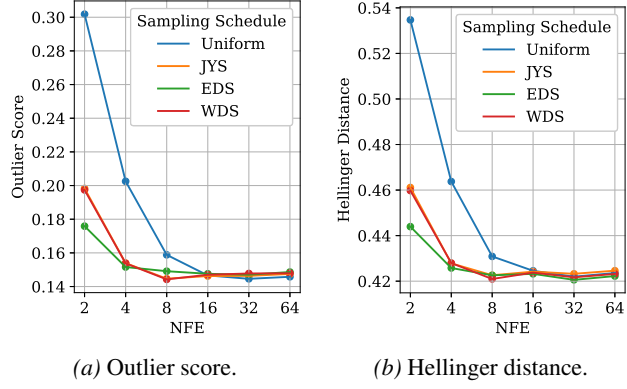


Figure 2. Performance comparisons on piano note generation across different metrics.

5.4. CIFAR-10

We evaluate our sampling schedules on the image domain using the CIFAR-10 model from Sahoo et al. (2024), which utilizes an absorbing state transition matrix and denoising parameterization. For this experiment, images are represented as flattened sequences of $3 \times 32 \times 32$ tokens with values in $\{0, \dots, 255\}$.

Figure 4 illustrates the Frechet Inception Distance (FID) scores (Heusel et al., 2017) (lower is better) as a function of NFEs. We observe that our schedules consistently improve upon the uniform baseline across all computational budgets. The gap is significant: **EDS** achieves the same performance as the baseline at 128 NFEs while using $4 \times$ fewer NFEs. **EDS** is the superior method in this setting, outperforming **WDS**. These quantitative findings are corroborated by the qualitative illustration in Figure 5. This advantage is most pronounced at lower NFEs (16–64): while the uniform schedule yields highly noisy outputs in this regime, our method generates structurally coherent images even with very few NFEs.

5.5. LANGUAGE MODELING

We evaluate our method on text generation using the Open-WebText dataset (Gokaslan et al., 2019). We employ pre-trained models from Lou et al. (2024) across two architecture sizes (SEDD-Small and SEDD-Medium), as well as the MDLM model from Sahoo et al. (2024). These models utilize absorbing diffusion dynamics parameterized

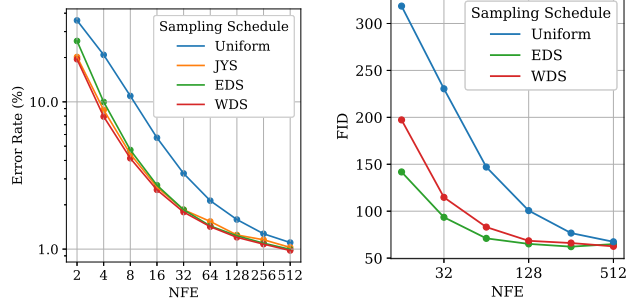


Figure 3. Performance comparison on the Countdown dataset.

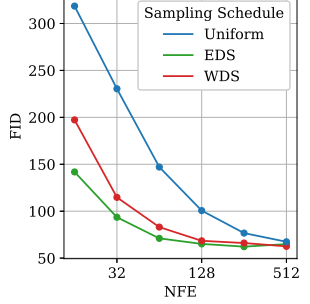


Figure 4. Performance comparison on CIFAR-10 (MDLM).

via a denoising entropic score (Lou et al., 2024) or a Rao-Blackwellized objective (Sahoo et al., 2024). We apply our **EDS** and **WDS** schedules, derived by computing the neural non-adiabatic entropy and practical Wasserstein bound, respectively, using a representative batch of 1,024 samples from the OpenWebText training set. Following the evaluation protocol of Lou et al. (2024), we generate 1,024 sequences of length 1,024 and measure generative perplexity (lower is better) using GPT-2 Large (Radford et al., 2019).

The results presented in Figure 6 demonstrate distinct performance characteristics for our proposed schedules across model scales. For SEDD-Small, SEDD-Medium, and MDLM, the **WDS** schedule consistently achieves the lowest generative perplexity, outperforming all alternatives including Uniform and JYS at all computational budgets. Conversely, we observe that the **EDS** schedule performs worse than other methods on SEDD models, although it performs well on MDLM after 64 NFEs. This discrepancy suggests that the geometric transport metric underlying **WDS** aligns effectively with the semantics of text generation and generalizes across modalities, demonstrating greater robustness and consistency compared to **EDS**.

6. Conclusion

In this work, we presented an improved sampling framework that achieves a superior compute-budget performance trade-off. This was achieved by bridging non-equilibrium thermodynamics and optimal transport geometry within the context of discrete generative modeling. We demonstrated that by applying thermodynamic principles to compute the non-adiabatic entropy production, we can characterize how the reverse process evolves in terms of information rate. Furthermore, we derived a practical bound on the Wasserstein velocity to measure the geometric evolution of intermediate steps toward the final generation.

Motivated by the observation that information flow in the generative reverse process is highly non-linear and dependent on both the data and the diffusion kernel, we proposed



Figure 5. CIFAR-10 generation results across different sampling schedules: Uniform (left), EDS (center), and WDS (right). Each row shows samples generated with different NFEs.

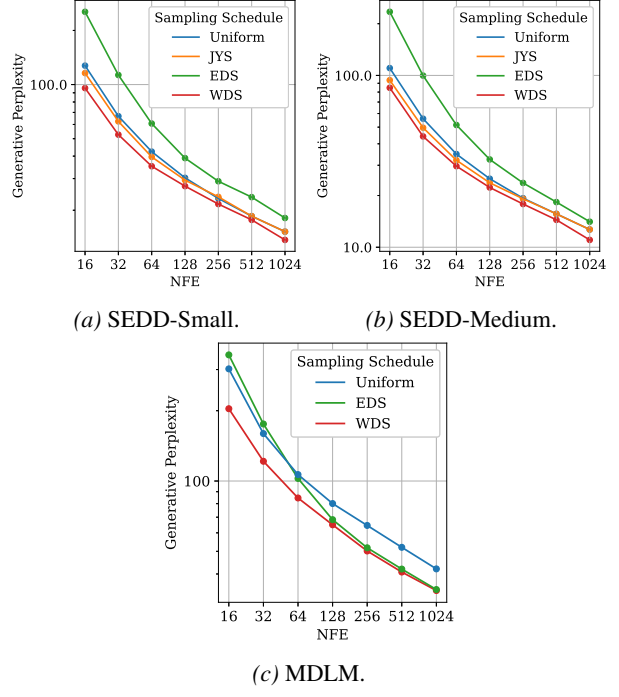


Figure 6. Performance comparisons on text generation across different models.

two intrinsic scheduling strategies: **EDS**, based on non-adiabatic entropy production, and **WDS**, derived from a geometric transport bound. Our analysis established that standard uniform schedules are often inefficient, disproportionately allocating computational steps to regimes with minimal information gain. To address this, we derived improved schedules by uniformly sampling timesteps within the intrinsic space of non-adiabatic entropy or Wasserstein distance, rather than in linear time.

Empirically, our method requires no additional training and generalizes across diverse modalities. Both **EDS** and **WDS** demonstrated significant efficiency gains, achieving high-fidelity generation at a fraction of the function evaluations required by uniform baselines. Notably, **WDS** proved particularly robust, consistently achieving the lowest perplexity and surpassing existing error-based schedules.

Ultimately, our findings confirm that the “physical time” of a diffusion process rarely aligns with its “semantic progress.” By realigning the sampling trajectory to the model’s intrinsic dynamics, we offer a plug-and-play solution that significantly enhances the inference efficiency of discrete diffusion models.

Impact Statement

This paper presents work whose goal is to advance the field of machine learning. There are many potential societal

consequences of our work, none of which we feel must be specifically highlighted here.

References

Anderson, W. J. *Continuous-time Markov chains: An applications-oriented approach*. Springer Science & Business Media, 2012.

Arriola, M., Sahoo, S. S., Gokaslan, A., Yang, Z., Qi, Z., Han, J., Chiu, J. T., and Kuleshov, V. Block diffusion: Interpolating between autoregressive and diffusion language models. In *The Thirteenth International Conference on Learning Representations*, 2025.

Austin, J., Johnson, D. D., Ho, J., Tarlow, D., and Van Den Berg, R. Structured denoising diffusion models in discrete state-spaces. *Advances in Neural Information Processing Systems*, 34:17981–17993, 2021.

Bao, F., Nie, S., Xue, K., Li, C., Pu, S., Wang, Y., Yue, G., Cao, Y., Su, H., and Zhu, J. One transformer fits all distributions in multi-modal diffusion at scale. In *International Conference on Machine Learning*, pp. 1692–1717. PMLR, 2023.

Ben-Hamu, H., Gat, I., Severo, D., Nolte, N., and Karrer, B. Accelerated sampling from masked diffusion models via entropy bounded unmasking. *arXiv preprint arXiv:2505.24857*, 2025.

Bounoua, M., Franzese, G., and Michiardi, P. Multi-modal latent diffusion. *arXiv preprint arXiv:2306.04445*, 2023.

Bounoua, M., Franzese, G., and Michiardi, P. S Ω i: Score-based o-INFORMATION estimation. In *Forty-first International Conference on Machine Learning*, 2024.

Bounoua, M., Franzese, G., and Michiardi, P. Learning to match unpaired data with minimum entropy coupling. In *Forty-second International Conference on Machine Learning*, 2025.

Campbell, A., Benton, J., De Bortoli, V., Rainforth, T., Deligiannidis, G., and Doucet, A. A continuous time framework for discrete denoising models. *Advances in Neural Information Processing Systems*, 35:28266–28279, 2022.

Chen, C., Ding, H., Sisman, B., Xu, Y., Xie, O., Yao, B. Z., Tran, S. D., and Zeng, B. Diffusion models for multi-modal generative modeling. *arXiv preprint arXiv:2407.17571*, 2024.

Chen, T. On the importance of noise scheduling for diffusion models. *arXiv preprint arXiv:2301.10972*, 2023.

Dong, H.-W., Hsiao, W.-Y., Yang, L.-C., and Yang, Y.-H. Musegan: Multi-track sequential generative adversarial networks for symbolic music generation and accompaniment. In *Proceedings of the AAAI conference on artificial intelligence*, 2018.

Esposito, M. and Van den Broeck, C. Three detailed fluctuation theorems. *Physical review letters*, 104(9):090601, 2010.

Foresti, A., Franzese, G., and Michiardi, P. Info-sedd: Continuous time markov chains as scalable information metrics estimators. *arXiv preprint arXiv:2502.19183*, 2025.

Franzese, G., Bounoua, M., and Michiardi, P. Minde: Mutual information neural diffusion estimation. *arXiv preprint arXiv:2310.09031*, 2023.

Fu, F., Guo, T., and Liu, Z. Learnable sampler distillation for discrete diffusion models. *arXiv preprint arXiv:2509.19962*, 2025.

Gokaslan, A., Cohen, V., Pavlick, E., and Tellex, S. Openwebtext corpus, 2019.

Hatano, T. and Sasa, S.-i. Steady-state thermodynamics of langevin systems. *Physical review letters*, 86(16):3463, 2001.

Heusel, M., Ramsauer, H., Unterthiner, T., Nessler, B., and Hochreiter, S. Gans trained by a two time-scale update rule converge to a local nash equilibrium. *Advances in neural information processing systems*, 30, 2017.

Ho, J., Jain, A., and Abbeel, P. Denoising diffusion probabilistic models. In Larochelle, H., Ranzato, M., Hadsell, R., Balcan, M., and Lin, H. (eds.), *Advances in Neural Information Processing Systems*, volume 33, pp. 6840–6851. Curran Associates, Inc., 2020.

Ho, J., Salimans, T., Gritsenko, A., Chan, W., Norouzi, M., and Fleet, D. J. Video diffusion models. *Advances in neural information processing systems*, 35:8633–8646, 2022.

Karras, T., Aittala, M., Aila, T., and Laine, S. Elucidating the design space of diffusion-based generative models. In Oh, A. H., Agarwal, A., Belgrave, D., and Cho, K. (eds.), *Advances in Neural Information Processing Systems*, 2022.

Kelly, F. P. Reversibility and stochastic networks. *PF Kelly—New York: Willy*, 1981.

Kim, J., Shah, K., Kontonis, V., Kakade, S., and Chen, S. Train for the worst, plan for the best: Understanding token ordering in masked diffusions. *arXiv preprint arXiv:2502.06768*, 2025.

Kong, X., Brekelmans, R., and Ver Steeg, G. Information-theoretic diffusion. In *International Conference on Learning Representations*, 2022.

Kong, Z., Ping, W., Huang, J., Zhao, K., and Catanzaro, B. Diffwave: A versatile diffusion model for audio synthesis. *arXiv preprint arXiv:2009.09761*, 2020.

Lezama, J., Salimans, T., Jiang, L., Chang, H., Ho, J., and Essa, I. Discrete predictor-corrector diffusion models for image synthesis. In *The Eleventh International Conference on Learning Representations*, 2022.

Li, X., Zhao, Y., Wang, C., Scalia, G., Eraslan, G., Nair, S., Biancalani, T., Ji, S., Regev, A., Levine, S., et al. Derivative-free guidance in continuous and discrete diffusion models with soft value-based decoding. *arXiv preprint arXiv:2408.08252*, 2024.

Lou, A., Meng, C., and Ermon, S. Discrete diffusion modeling by estimating the ratios of the data distribution. *stat*, 1050:21, 2024.

Nisonoff, H., Xiong, J., Allenspach, S., and Listgarten, J. Unlocking guidance for discrete state-space diffusion and flow models. *arXiv preprint arXiv:2406.01572*, 2024.

Park, Y.-H., Lai, C.-H., Hayakawa, S., Takida, Y., and Mitsu-fuji, Y. Jump your steps: Optimizing sampling schedule of discrete diffusion models. In *The Thirteenth International Conference on Learning Representations*, 2024.

Premkumar, A. Neural entropy. *arXiv preprint arXiv:2409.03817*, 2024.

Radford, A., Wu, J., Child, R., Luan, D., Amodei, D., Sutskever, I., et al. Language models are unsupervised multitask learners. *OpenAI blog*, 1(8):9, 2019.

Raffel, C. *Learning-based methods for comparing sequences, with applications to audio-to-midi alignment and matching*. Columbia University, 2016.

Ramesh, A., Pavlov, M., Goh, G., Gray, S., Voss, C., Radford, A., Chen, M., and Sutskever, I. Zero-shot text-to-image generation. In *International conference on machine learning*, pp. 8821–8831. Pmlr, 2021.

Ren, Y., Chen, H., Zhu, Y., Guo, W., Chen, Y., Rotskoff, G. M., Tao, M., and Ying, L. Fast solvers for discrete diffusion models: Theory and applications of high-order algorithms. *arXiv preprint arXiv:2502.00234*, 2025.

Rombach, R., Blattmann, A., Lorenz, D., Esser, P., and Ommer, B. High-resolution image synthesis with latent diffusion models. In *Proceedings of the IEEE/CVF Conference on Computer Vision and Pattern Recognition (CVPR)*, pp. 10684–10695, June 2022.

Sahoo, S. and Kuleshov, V. MuLAN: Multivariate learned adaptive noise. In *Advances in Neural Information Processing Systems (NeurIPS)*, 2024. [7].

Sahoo, S., Arriola, M., Schiff, Y., Gokaslan, A., Marroquin, E., Chiu, J., Rush, A., and Kuleshov, V. Simple and effective masked diffusion language models. *Advances in Neural Information Processing Systems*, 37:130136–130184, 2024.

Schiff, Y., Kao, C.-H., Gokaslan, A., Dao, T., Gu, A., and Kuleshov, V. Caduceus: Bi-directional equivariant long-range dna sequence modeling. *arXiv preprint arXiv:2403.03234*, 2024a.

Schiff, Y., Sahoo, S. S., Phung, H., Wang, G., Boshar, S., Dalla-torre, H., de Almeida, B. P., Rush, A., Pierrot, T., and Kuleshov, V. Simple guidance mechanisms for discrete diffusion models. *arXiv preprint arXiv:2412.10193*, 2024b.

Seifert, U. Entropy production along a stochastic trajectory and an integral fluctuation theorem. *Physical review letters*, 95(4):040602, 2005.

Sohl-Dickstein, J., Weiss, E., Maheswaranathan, N., and Ganguli, S. Deep unsupervised learning using nonequilibrium thermodynamics. In Bach, F. and Blei, D. (eds.), *Proceedings of the 32nd International Conference on Machine Learning*, volume 37 of *Proceedings of Machine Learning Research*, pp. 2256–2265, Lille, France, 07–09 Jul 2015. PMLR.

Song, Y., Sohl-Dickstein, J., Kingma, D. P., Kumar, A., Ermon, S., and Poole, B. Score-based generative modeling through stochastic differential equations. In *International Conference on Learning Representations*, 2021.

Stancevic, D., Handke, F., and Ambrogioni, L. Entropic time schedulers for generative diffusion models. *arXiv preprint arXiv:2504.13612*, 2025.

Sun, H., Yu, L., Dai, B., Schuurmans, D., and Dai, H. Score-based continuous-time discrete diffusion models, 2023. URL <https://arxiv.org/abs/2211.16750>.

Van Vu, T. and Saito, K. Thermodynamic unification of optimal transport: Thermodynamic uncertainty relation, minimum dissipation, and thermodynamic speed limits. *Physical Review X*, 13(1):011013, 2023.

Vaswani, A., Shazeer, N., Parmar, N., Uszkoreit, J., Jones, L., Gomez, A. N., Kaiser, Ł., and Polosukhin, I. Attention is all you need. *Advances in neural information processing systems*, 30, 2017.

Yoshimura, K., Kolchinsky, A., Dechant, A., and Ito, S.
Housekeeping and excess entropy production for general nonlinear dynamics. *Physical Review Research*, 5(1), January 2023. ISSN 2643-1564. doi: 10.1103/physrevresearch.5.013017.

Zhao, Y., Shi, J., Chen, F., Druckmann, S., Mackey, L., and Linderman, S. Informed correctors for discrete diffusion models. *arXiv preprint arXiv:2407.21243*, 2024.

A. Additional details

A.1. Discrete Diffusion

In this work, we consider two types of discrete diffusion processes based on their transition rate matrix Q : absorbing state discrete diffusion and uniform discrete diffusion. The difference in Q is highlighted by Figure 7.

Figure 7. Transition rate matrices for discrete diffusion. The absorb matrix (left) represents transitions from data states to a specific mask token, while the uniform matrix (right) allows transitions between all N states with equal probability.

A.2. Total entropy production

We derive the total entropy production \mathcal{H}^{tot} for the reverse process, mapping each step to the corresponding thermodynamic definition in (Yoshimura et al., 2023).

First, we define the thermodynamic force for a transition from state x to y . In our notation, the forward flux is $\mathcal{K}_{(x,y)} = \overleftarrow{p}_t(x)\overleftarrow{Q}_t(x,y)$. The thermodynamic force is the log-ratio of the forward and reverse fluxes:

$$F_{(x,y)}(t) = \ln \frac{\overleftarrow{p}_t(x)\overleftarrow{Q}_t(x,y)}{\overleftarrow{p}_t(y)\overleftarrow{Q}_t(y,x)}. \quad (15)$$

This formulation is equivalent to Eq. (8) in the original paper, where $F_e(x) = \ln(\mathcal{K}_e(x)/\mathcal{K}_{-e}(x))$ (Yoshimura et al., 2023).

The entropy production rate $\mathcal{H}^{\text{tot}}(t)$ is defined as the sum of the product of currents and forces. In the continuous-time limit, this is equivalent to the sum of fluxes multiplied by the force:

$$\mathcal{H}^{\text{tot}}(t) = \sum_{x,y \in \chi} \overleftarrow{p}_t(x) \overleftarrow{Q}_t(x,y) \ln \frac{\overleftarrow{p}_t(x) \overleftarrow{Q}_t(x,y)}{\overleftarrow{p}_t(y) \overleftarrow{Q}_t(y,x)}. \quad (16)$$

This corresponds to *Eq. (9)* in (Yoshimura et al., 2023).

We apply the standard CTMC time-reversal identity. The reverse generator \overleftarrow{Q} relates to the forward generator \overrightarrow{Q} via:

$$\overleftarrow{p}_t(y)\overleftarrow{Q}_t(y, x) = \overrightarrow{p}_{T-t}(x)\overrightarrow{Q}_{T-t}(x, y). \quad (17)$$

Substituting this into the denominator of the log term in the EPR equation allows us to express the entropy in terms of the reconstruction trajectory.

The total entropy is obtained by integrating the entropy production rate $\mathcal{H}^{\text{tot}}(t)$ over the time interval $[0, T]$. By applying the substitution from Step 3, we arrive at the final form:

$$\mathcal{H}^{\text{tot}} = \int_0^T \sum_{x,y} \overleftarrow{p}_t(x) \overleftarrow{Q}_t(x,y) \ln \left(\frac{\overleftarrow{p}_t(x) \overleftarrow{Q}_t(x,y)}{\overrightarrow{p}_{T-t}(y) \overrightarrow{Q}_{T-t}(x,y)} \right) dt. \quad (18)$$

A.3. Decomposition of the total entropy production

The decomposition follows from an explicit expansion of the logarithmic ratio of forward and backward path probabilities (Esposito & Van den Broeck, 2010; Hatano & Sasa, 2001).

For the reverse CTMC with time-dependent generator \overleftarrow{Q}_t and instantaneous stationary distribution π_t (such that $\pi_t \overleftarrow{Q}_t = 0$), the corresponding entropy production rates read:

$$\mathcal{H}^{\text{ad}}(t) = \sum_{x,y} \overleftarrow{p}_t(x) \overleftarrow{Q}_t(x,y) \ln \frac{\overleftarrow{Q}_t(x,y) \pi_t(x)}{\overleftarrow{Q}_t(y,x) \pi_t(y)}, \quad (19)$$

$$\mathcal{H}^{\text{na}}(t) = \sum_{x,y} \overleftarrow{p}_t(x) \overleftarrow{Q}_t(x,y) \ln \frac{\overleftarrow{p}_t(x) \pi_t(y)}{\overleftarrow{p}_t(y) \pi_t(x)}. \quad (20)$$

Summing these two components yields the instantaneous total entropy production rate \mathcal{H}^{tot} . The terms involving π_t cancel out:

$$\mathcal{H}^{\text{ad}}(t) + \mathcal{H}^{\text{na}}(t) = \sum_{x,y} \overleftarrow{p}_t(x) \overleftarrow{Q}_t(x,y) \ln \frac{\overleftarrow{p}_t(x) \overleftarrow{Q}_t(x,y)}{\overleftarrow{p}_t(y) \overleftarrow{Q}_t(y,x)}. \quad (21)$$

By applying the time-reversal where $\overleftarrow{p}_t(y) \overleftarrow{Q}_t(y,x) = \overrightarrow{p}_{T-t}(x) \overrightarrow{Q}_{T-t}(x,y)$, we recover the exact form of the total entropy derived previously in Equation (1):

$$\mathcal{H}^{\text{ad}}(t) + \mathcal{H}^{\text{na}}(t) = \sum_{x,y} \overleftarrow{p}_t(x) \overleftarrow{Q}_t(x,y) \ln \frac{\overleftarrow{p}_t(x) \overleftarrow{Q}_t(x,y)}{\overrightarrow{p}_{T-t}(y) \overrightarrow{Q}_{T-t}(y,x)}. \quad (22)$$

A.4. Wasserstein bound

Here we provide additional details about the Wasserstein bound discussed in the main text. The dynamical state mobility is defined following (Van Vu & Saito, 2023).

$$\mathcal{M}(t) \stackrel{\text{def}}{=} \sum_{x,y} \frac{\overleftarrow{Q}_t(x,y) \overleftarrow{p}_t(y) - \overleftarrow{Q}_t(y,x) \overleftarrow{p}_t(x)}{\log \overleftarrow{Q}(x,y) \overleftarrow{p}_t(y) - \log \overleftarrow{Q}_t(y,x) \overleftarrow{p}_t(x)}. \quad (23)$$

Conveniently, Van Vu & Saito (2023) show that $\mathcal{M}(t) \leq \frac{\mathcal{A}(t)}{2}$, where $\mathcal{A}(t)$ is simply $\sum_{x,y} \overleftarrow{Q}(x,y) \overleftarrow{p}_t(y)$.

It follows that we can obtain another bound based on $\mathcal{A}(t)$:

$$\mathcal{W}_1(\overleftarrow{p}_0, \overleftarrow{p}_T) \leq \int_0^T \sqrt{\mathcal{A}(t) \mathcal{H}^{\text{tot}}(t)} dt. \quad (24)$$

While the bound in Equation (24) is looser than the bound in Equation (5), the former turns out to be numerically more stable in practical applications.

For masked dynamics, total entropy production diverges due to irreversibility, rendering standard bounds uninformative. However, probability transport remains finite and is driven primarily by the *non-adiabatic* entropy production (Yoshimura et al., 2023). Specifically, Yoshimura et al. (2023) derive a thermodynamic uncertainty relation (Eq. H.10) bounding the Wasserstein distance:

$$\mathcal{W}_1(\overleftarrow{p}_0, \overleftarrow{p}_T) \leq \sqrt{\frac{1}{2} \left(\int_0^T \mathcal{A}(t) dt \right) \left(\int_0^T \mathcal{H}^{\text{na}}(t) dt \right)}. \quad (25)$$

Motivated by this, we introduce the practical bound $\int_0^T \sqrt{\mathcal{A}(t) \mathcal{H}^{\text{na}}(t)} dt$. This metric refines Equation (25) and serves as a stable proxy for $\mathcal{W}_\theta(p_0, p_T)$ by utilizing only the finite non-adiabatic term. It naturally generalizes Equation (24); for reversible dynamics (e.g., uniform diffusion), the adiabatic term vanishes, and our metric recovers the standard total entropy production.

A.5. Derivation of the Non adiabatic Entropy Estimator

To estimate the non-adiabatic entropy production $\mathcal{H}_\theta^{\text{na}}(t)$ using a neural network, we express the probability ratio in terms of the learned score. The score network $s_\theta^p(x, y)$ is typically trained to approximate the forward transition ratio:

$$s_\theta^p(x, y) \approx \frac{\overrightarrow{p}_{T-t}(y)}{\overrightarrow{p}_{T-t}(x)} = \frac{\overleftarrow{p}_t(y)}{\overleftarrow{p}_t(x)}. \quad (26)$$

Substituting the inverse relationship $\frac{\overleftarrow{p}_t(x)}{\overleftarrow{p}_t(y)} \approx s_\theta^p(x, y)^{-1}$ into the expression for $\mathcal{H}_\theta^{\text{na}}(t)$, we obtain the instantaneous estimator:

$$\mathcal{H}_\theta^{\text{na}}(t) = \sum_{x, y} \overleftarrow{p}_t(x) \overleftarrow{Q}_t(x, y) \left[-\ln s_\theta^p(x, y) + \ln \frac{\pi_t(y)}{\pi_t(x)} \right]. \quad (27)$$

The total non-adiabatic entropy production, $\mathcal{H}_\theta^{\text{na}}$, is obtained by integrating this rate over the generation interval $[0, T]$:

$$\mathcal{H}_\theta^{\text{na}} = \int_0^T \mathbb{E}_{x \sim \overleftarrow{p}_t} \left[\sum_y \overleftarrow{Q}_t(x, y) \left(-\ln s_\theta^p(x, y) + \ln \frac{\pi_t(y)}{\pi_t(x)} \right) \right] dt. \quad (28)$$

Assuming the stationary distribution terms vanish (as in uniform or absorbing diffusion).

$$\mathcal{H}_\theta^{\text{na}} = - \int_0^T \mathbb{E}_{x \sim \overleftarrow{p}_t} \left[\sum_y \overleftarrow{Q}_t(x, y) \ln s_\theta^p(x, y) \right] dt. \quad (29)$$

A.6. Technical details

For all experiments, we adhere to the procedure in Algorithm 1, which requires evaluating the neural non-adiabatic entropy. To achieve this, we use N samples from the training dataset and evaluate them across N_τ timestamppdf uniformly sampled from $[0, T]$ to estimate the entropy rate. The Wasserstein bound is derived in a similar manner. We then proceed according to the methodology described in Section 4. The derived time schedule is sampler-agnostic. For all our experiments, we utilize the Euler τ -leaping sampler (Campbell et al., 2022). In Table 1, we report the parameters N and N_τ used for our empirical validation.

Table 1. Parameters used for estimating the neural non-adiabatic entropy across different datasets.

Dataset	Samples (N)	Timestamppdf (N_t)
Binomial Distribution	1024	1024
Count Dataset	1024	1024
Monophonic Music	64	1024
CIFAR-10	64	1024
Language Modeling	64	1024

As our method is training-free, it relies exclusively on pre-trained model checkpoints. In all our experiments, we prioritize using pre-trained models from the official codebase of Park et al. (2024); where these are unavailable, we train the models using their provided scripts. For MDLM, we utilize the official codebase and pre-trained weights from Sahoo & Kuleshov (2024), with the exception of the CIFAR experiment, which uses the MDLM implementation from Schiff et al. (2024b). We compare our method against JYS (Sahoo & Kuleshov, 2024) in all experiments, excluding the MDLM-based text and CIFAR tasks. In these specific cases, the JYS baseline was omitted due to the unavailability of a compatible implementation for these diffusion settings.

B. Additional Results

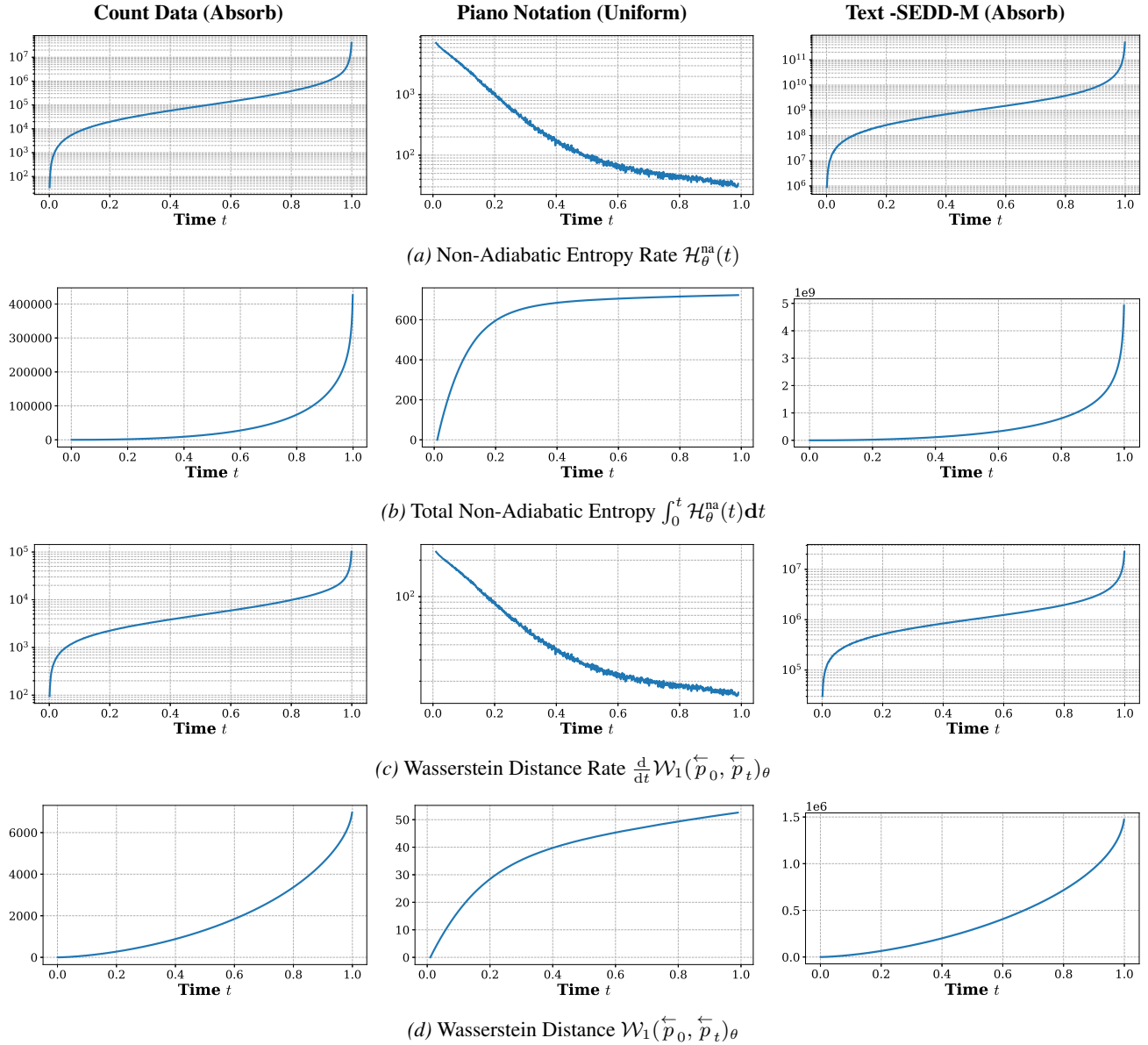


Figure 8. Detailed breakdown of entropy and transport dynamics across three modalities: Count data (left), Piano notation (center), and Text generation (right). Each row visualizes a specific metric: (a) Non-adiabatic entropy rate, (b) Total Non-adiabatic entropy production, (c) Wasserstein distance rate and (d) Wasserstein distance.

C. Generated Samples

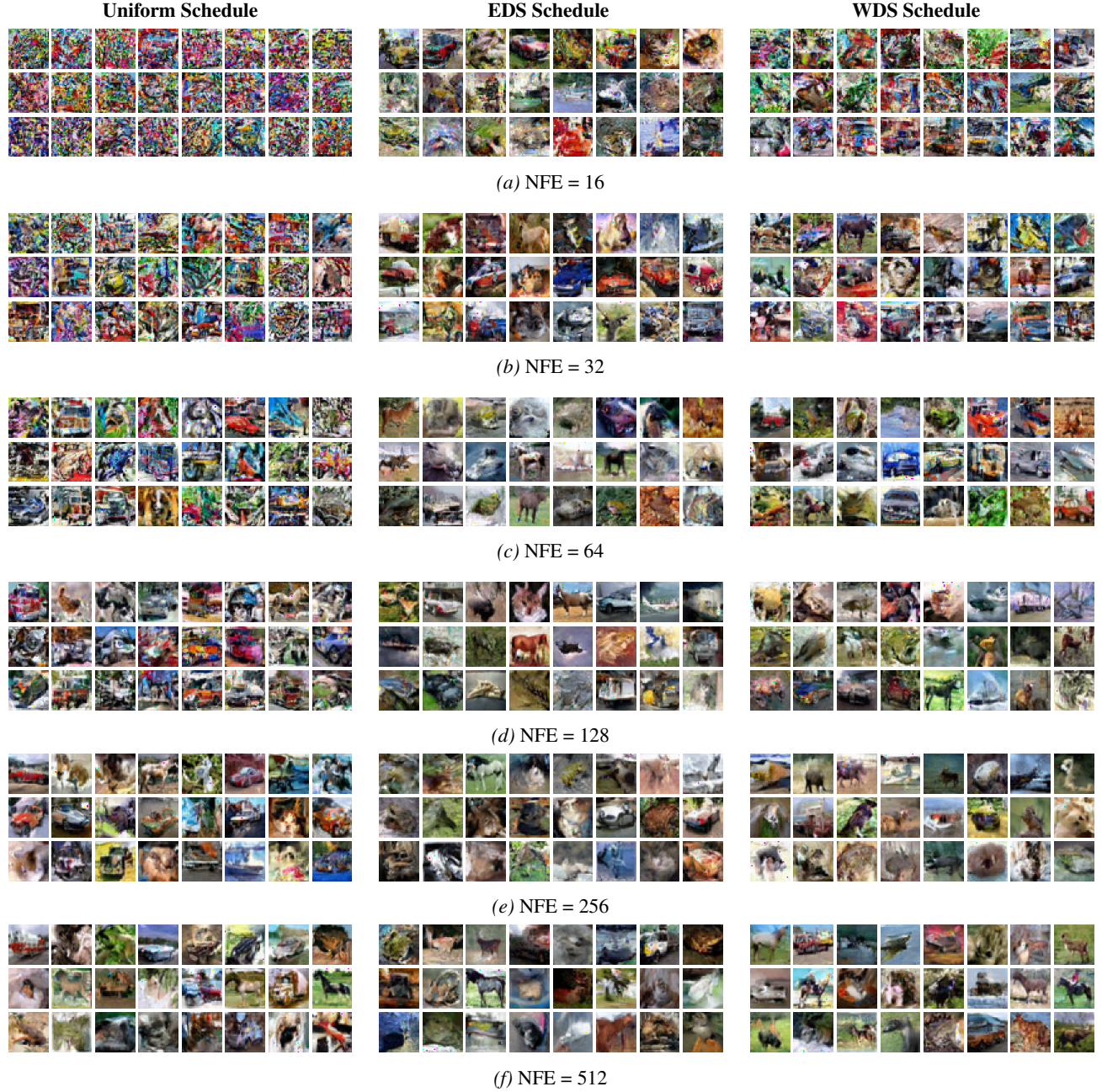


Figure 9. CIFAR-10 generation results across different sampling schedules: Uniform (left), EDS (center), and WDS (right). Each row shows samples generated at varying NFEs, demonstrating the efficiency and quality trade-offs for each scheduling method.